In situ control of hole-spin driving mechanisms

Simon Geyer,[1,*] Rafael S. Eggli,[1,*] Carlos Dos Santos,[1] Miguel J. Carballido,[1,†] Peter Stano,[2,3] Daniel Loss,[1,2,‡] Dominik M. Zumbühl,[1] Richard J. Warburton,[1] and Andreas V. Kuhlmann[1,§]
[1]*Department of Physics, University of Basel, Klingelbergstrasse 82, CH-4056 Basel, Switzerland*
[2]*RIKEN, Center for Quantum Computing (RQC), 2-1 Hirosawa, Wako, Saitama 351-0198, Japan*
[3]*Institute of Physics, Slovak Academy of Sciences, 845 11 Bratislava, Slovakia*

(Received 22 December 2025; accepted 6 August 2026; published 21 September 2026)

Hole-spin qubits enable fast, all-electrical spin manipulation through electric-dipole spin resonance (EDSR), arising from two microscopic mechanisms rooted in their intrinsically strong spin-orbit interaction. Depending on how the electric field acts on the quantum dot, the spin can be driven either by a modulation of its *g* factor or by a displacement of the wavefunction. Here, we demonstrate *in situ* control over the dominant EDSR driving mechanism of a hole-spin qubit in a silicon fin field-effect transistor by applying microwave signals to two different gate electrodes, thereby tuning the orientation of the local electric field. We measure the effective *g* factor, its electrical tunability, and the Rabi frequency as functions of magnetic-field orientation. Their distinct angular dependencies, analyzed using a *g*-matrix formalism, allow us to identify the underlying driving processes and track their relative contributions for different drive configurations. By selecting the drive electrode, we can switch from a regime dominated by *g*-factor modulation to one with a strong contribution from wavefunction displacement. This *in situ* tunability provides direct experimental access to both spin-driving mechanisms and offers a route toward optimized spin-qubit performance.

DOI: 10.1103/f1hx-nk4s

I. INTRODUCTION

Spin qubits in semiconductor quantum dots (QDs) are promising candidates for high-fidelity, scalable quantum computing [1–11]. In comparison to electron spins, hole spins [12–22] can be controlled all-electrically via electric-dipole spin resonance (EDSR) [23–26], without the added complexity of on-chip micromagnets [27,28] or the need for an orbital degeneracy [29], thanks to their intrinsic spin-orbit interaction (SOI). In materials with strong SOI, such as holes in silicon (Si), the Larmor (spin precession) vector $\mathbf{f}_\mathrm{L}$ and magnetic field $\mathbf{B}$ are no longer related via a scalar g factor. Instead, a 3×3 g tensor $\hat{g}$ [18,19,30–32] is required, leading to $\mathbf{f}_\mathrm{L} = \mu_\mathrm{B}\hat{g}\mathbf{B}/h$, where μ_B is Bohr's magneton and h is Planck's constant. To induce spin rotations using EDSR, a periodic modulation of $\mathbf{f}_\mathrm{L}$ transverse to the spin quantization axis $\mathbf{n} = \hat{g}\mathbf{B}/|\hat{g}\mathbf{B}|$ must be applied close to the qubit's Larmor frequency $f_\mathrm{L} = |\mathbf{f}_\mathrm{L}|$.

This can be achieved through two fundamentally different mechanisms [33–35]. The first one is referred to as g-tensor modulation resonance (gTMR), in which a transverse modulation of the Larmor vector arises because an alternating (ac) electric field deforms the g tensor—either by rotating its principal axes or by changing its principal values in an anisotropic manner [36] [Fig. 1(f)]. Electrical control of $\hat{g}$ is enabled by SOI, primarily through changes in the heavy- and light-hole mixing [37] induced by the confinement potential [38], as well as by strain or strain gradients [32].

Second, coherent spin rotations can be driven by periodically displacing the QD as a whole with an ac electric field [23,39] [Fig. 1(g)]. In the presence of SOI, this motion generates an effective time-dependent magnetic field, resulting in a noncollinear modulation of the Larmor vector. For a quasiharmonic confinement, the hole wavefunction and the effective g factor $g^* = |\hat{g}\mathbf{B}|/|\mathbf{B}|$, and hence the Zeeman splitting $E_\mathrm{Z} = hf_\mathrm{L}$, remain unchanged during the motion. Therefore, this driving mechanism is called iso-Zeeman EDSR (IZR) [33].

In practice, the driving mechanisms typically coexist, and different relative weights of gTMR and IZR have been reported for various hole-spin-qubit devices [18,33,40]. To describe these mechanisms within a unified framework, the g-matrix formalism was developed [33–35], which enables the individual contributions to the observed Rabi drive to be disentangled.

The importance of the underlying driving mechanism is highlighted by an operational sweet spot with simultaneously maximized qubit drive speed and coherence [40] as a

[*]These authors contributed equally to this work.
[†]Present address: School of Electrical Engineering and Telecommunications, University of New South Wales, Sydney, NSW 2052, Australia.
[‡]Present address: Physics Department, King Fahd University of Petroleum and Minerals (KFUPM), 31261 Dhahran, Saudi Arabia; Center for Advanced Quantum Computing, KFUPM, Dhahran, Saudi Arabia; and RDIA Chair in Quantum Computing.
[§]Contact author: andreas.kuhlmann@unibas.ch

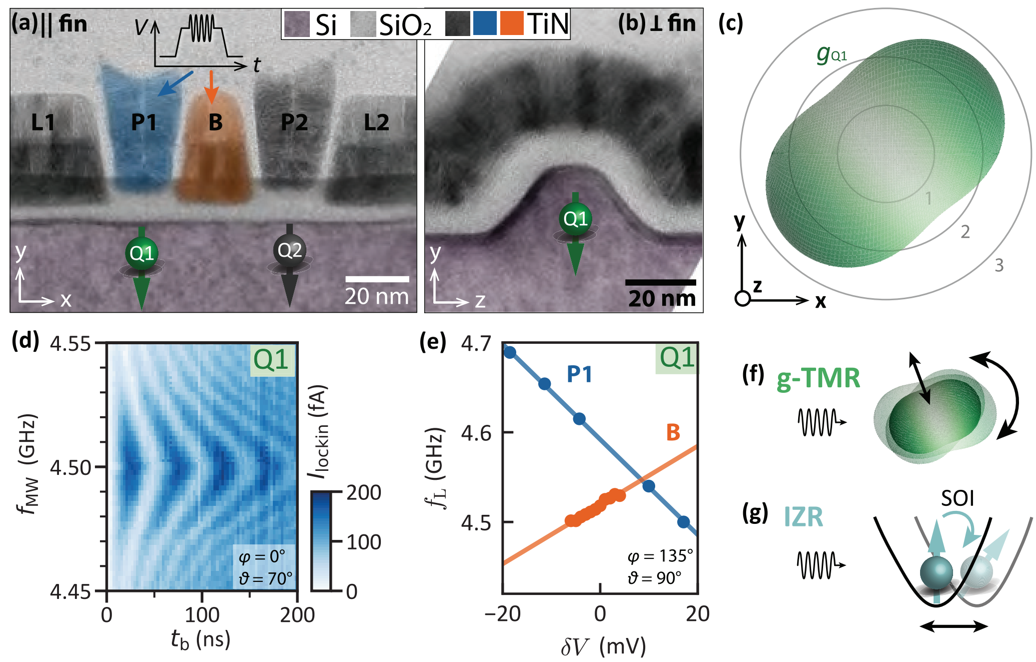

FIG. 1. Hole-spin-qubit anisotropies and driving mechanisms. (a) False-color transmission electron microscope (TEM) image of the measured device, showing the cross section along the fin direction. The qubits (Q1, Q2) are located beneath the plunger gates (P1, P2) and are manipulated by applying microwave signals to either P1 or the barrier gate B. The barrier voltage controls the interdot tunneling, and the lead gates (L1, L2) accumulate the hole reservoirs. The widths of the B and P gates are $\simeq 20$ nm. (b) Cross-sectional TEM image of a cofabricated device, highlighting the nearly triangular fin shape. (c) Projection of the g tensor onto the xy plane, showing a strong anisotropy. (d) Rabi chevron pattern of Q1 under P1 drive, demonstrating a Rabi frequency of $f_R = 20$ MHz on resonance. Data were taken at $B = 0.136$ T, $\phi = 0^\circ$, $\theta = 70^\circ$ (as defined in Fig. 2), and $V_{MW,P1} = 12$ mV. (e) The qubit Larmor frequency f_L of Q1 is tuned by the voltages applied to P1 and B. Data were taken at $B = 0.172$ T, $\phi = 135^\circ$, and $\theta = 90^\circ$. (f) and (g) Schematic illustrations of the gTMR and IZR driving mechanisms, respectively.

function of the static electric field, made possible by predominantly IZR-based driving. Likewise, hole spins can exhibit "reciprocal sweetness" [20,41,42], where qubit speed and coherence peak together as a function of the magnetic-field direction. While these results open promising avenues for qubit optimizations, *in situ* electrical control over the relative contributions of the two mechanisms to the overall Rabi frequency has not been achieved to date. Such control ultimately depends on how the microwave electric field couples to the QD [35], which in turn is determined by the layout of the gate electrodes and the geometry of the confinement potential. For example, driving from a more remote gate electrode [40] can promote a lateral displacement of the QD along the transport direction—the axis of weak confinement—in systems with strong biaxial confinement [12,16,39], thereby enhancing the IZR contribution. Experimental confirmation and quantification of how the relative position of the driving gate electrode with respect to the qubit affects the driving mechanism are therefore needed.

Here, we investigate the driving mechanisms of a hole-spin qubit in a silicon fin field-effect transistor (FinFET) [16,19,43–45], modeling the experimental results using the g-matrix formalism. By applying the microwave drive signal to two distinct gate electrodes, we achieve *in situ* control over the EDSR driving mechanism, tuning the system from a gTMR-dominated regime to one in which IZR contributes substantially to the Rabi frequency. These results demonstrate that the position of the driving gate relative to the qubit plays a decisive role in determining the dominant driving mechanism, opening opportunities for device designs that enable real-time, on-demand switching between gTMR and IZR operation. Finally, we discuss the physical origin of this tunability and its connection to sweet-spot operation.

II. EXPERIMENTAL SETUP

Two hole QDs are formed in the Si fin beneath plunger gates P1 and P2, each hosting an effective spin-1/2 qubit labeled Q1 and Q2 [see Fig. 1(a)]. The position of Q1 under P1 is evidenced by the charge stability maps [16,43,46], the strength of g-tensor tuning from voltages on P1 that differs greatly for Q1 and Q2 due to proximity [20], and the exponential control over the tunnel and exchange coupling achieved by the B gate [19]. The fin has a nearly triangular cross section [see Fig. 1(b)], which produces quasi-one-dimensional confinement of the holes and induces a strong direct-Rashba SOI [25,26]. A square pulse applied to P1 switches the device between Pauli spin blockade (PSB) [47], used for spin initialization and spin-parity readout via direct-current transport measurements, and Coulomb blockade [39]. In the latter regime, fast microwave bursts are applied for spin manipulation via EDSR. These bursts can be applied to either P1 or the barrier gate B. A difference in the effective g factors allows the two qubits to be addressed independently. To enhance spin readout contrast, we employ a lock-in detection scheme [12,16,19,22], yielding the signal $I_{lock-in}$. A three-axis

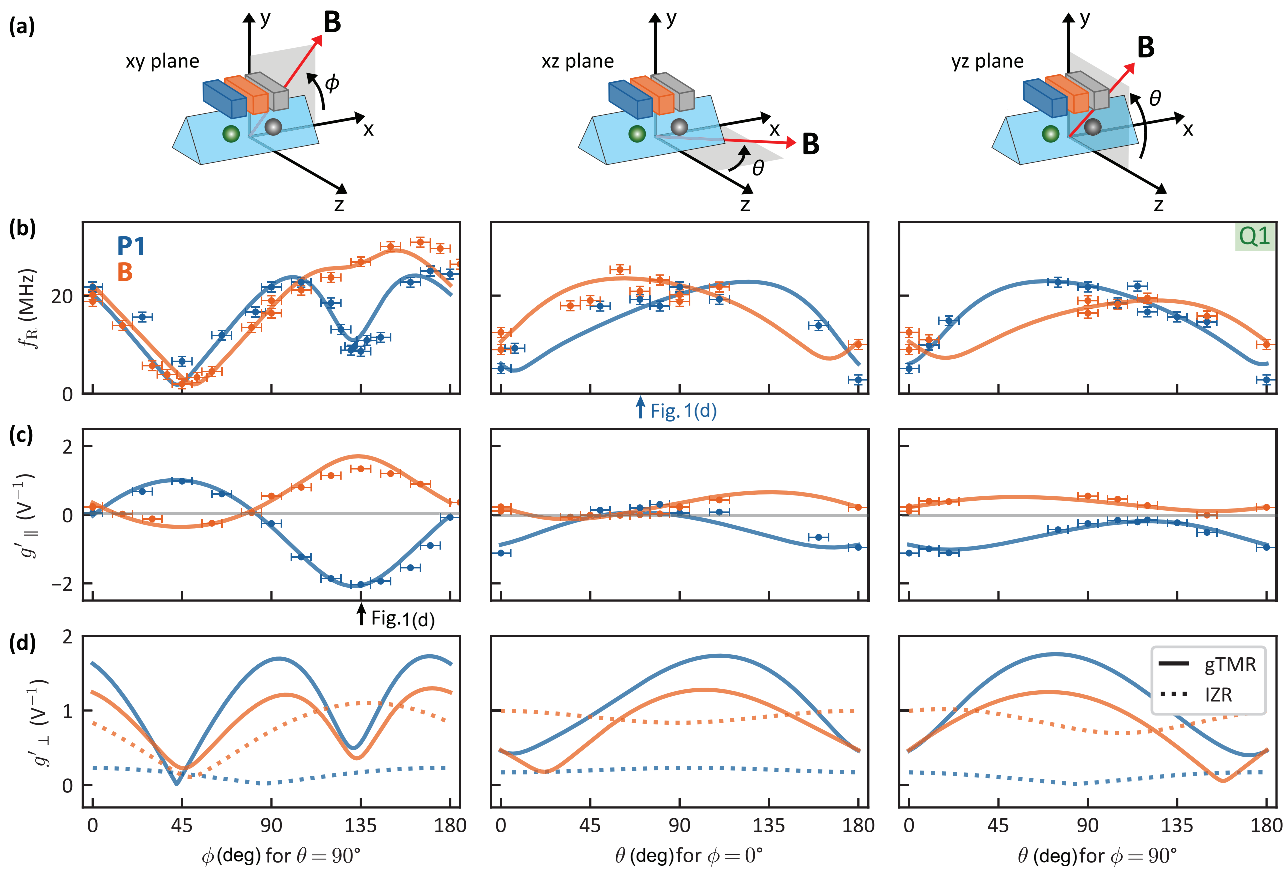

FIG. 2. Rabi drive anisotropy. (a) Schematic of the three magnetic-field planes used in the experiments, shown relative to the orientation of the Si fin (light blue) and the two driving gate electrodes (dark blue, orange). (b) Rabi frequency of Q1 under P1 (blue markers) and B driving (orange markers) as a function of magnetic-field orientation. Data were taken at fixed $f_L = 4.5$ GHz, $V_{MW,P1} = 12$ mV, and $V_{MW,B} = 13.5$ mV. Solid curves are fits based on the model described in the main text. The uncertainty in f_R is estimated as ± 1 MHz. (c) Electrical longitudinal tunability of the Q1 g factor as function of magnetic-field orientation for P1 (blue markers) and B driving (orange markers). Solid curves correspond to model fits of $\hat{g}'_{gTMR}$, projected onto the spin quantization axis and magnetic field as described in the main text. (d) Solid and dashed curves show the transverse components of $\hat{g}'$, as defined in the main text. The 1σ error bars in g' were obtained by propagating an estimated magnetic-field hysteresis of ± 5 mT. Gaps in the data are due to failing PSB readout for some magnetic-field orientations.

vector magnet enables experiments with an arbitrarily oriented magnetic field.

III. RESULTS

A. Anisotropy of the g tensor

We characterize $\hat{g}$ [30,31] of Q1 by probing its Zeeman splitting spectroscopically. As the orientation of **B** is varied, the anisotropy of $\hat{g}$ [32,48–51] appears through $E_Z = \mu_B|\hat{g}\mathbf{B}|$ (Fig. S1 of the Supplemental Material [52]) [19]. Using the procedure of Crippa *et al.* [33] (Sec. A of the Supplemental Material [52]), we obtain

$$\hat{g} = \begin{pmatrix} 2.38 & 0.52 & -0.01 \\ 0.52 & 2.22 & 0.01 \\ -0.01 & 0.01 & 1.58 \end{pmatrix}, \quad (1)$$

as visualized in Fig. 1(c). Although $\hat{g}$ contains nine elements, spectroscopy provides access only to the magnitude of the effective Zeeman field $|\hat{g}\mathbf{B}|$, not its direction. Consequently, only six independent parameters can be determined: three principal g factors, which set the Zeeman splitting along the principal magnetic axes, and three Euler angles specifying their orientation [19,32,33]. The remaining three degrees of freedom correspond to an arbitrary rotation in spin space—equivalently, a unitary transformation of the Kramers basis—which leaves $|\hat{g}\mathbf{B}|$ and thus all observables invariant [33,41].

In the following, we present the results for Q1; a corresponding analysis for Q2 is given in Secs. B and F of the Supplemental Material [52]. We also compare the extracted g tensor with a microscopic model (Sec. C of the Supplemental Material [52]), which offers a physical interpretation of the observed anisotropy.

B. Anisotropy of the Rabi frequency

Next, we drive Q1 for a variable burst duration t_b from P1 using a microwave amplitude $V_{MW,P1} = 12$ mV and a frequency f_{MW} close to $f_L = 4.5$ GHz [Fig. 1(d)]. The Rabi frequency f_R is extracted by fitting $I_{lock\text{-}in}$ at resonance as a function of t_b, and this procedure is repeated for different magnetic-field orientations in the three planes shown in Fig. 2(a). The resulting data [Fig. 2(b), blue markers] reveal a pronounced angular dependence of f_R, with certain orientations exhibiting strongly suppressed Rabi driving (e.g., $\phi \simeq 45^\circ,\ \theta = 90^\circ$). Driving the qubit from the barrier gate B with $V_{\rm MW,B} = 13.5$ mV instead leads to a markedly different anisotropy [Fig. 2(b), orange markers]. Absolute values of $V_{\rm MW}$ were chosen to approximately match power transfer to the qubit while respecting limits imposed by the transport-based readout. To understand these differences in the $f_{\rm R}$ anisotropies, we now examine the underlying EDSR driving mechanisms.

If the driving electric field distorts the QD's confinement potential, it can deform the g tensor, giving rise to gTMR-driven spin rotations [36,53]. The magnitude of the g-factor tunability, defined as $g' = \partial g/\partial V$, is determined by measuring the linear response of $f_{\rm L}$ to small gate-voltage changes δV [Fig. 1(e)]. Note the opposite sign of g' for voltages on B versus P1, similar to earlier reports [40,54]. Together with the measured $\hat{g}$ and the drive amplitude $V_{\rm MW}$, the matrix describing this tunability—denoted as the "gTMR-induced component of the g-derivative," $\hat{g}'_{\rm gTMR}$—fully specifies the gTMR-induced Rabi frequency $f_{\rm R,gTMR}$ [40] for any magnetic-field orientation [33].

In contrast, IZR originates from a displacement of the QD in a system with SOI [23,39], while the confinement potential and therefore g^* and $E_{\rm Z}$ remain unchanged. Within the g-matrix formalism [33,34,55], IZR accounts for the difference between the experimentally observed $f_{\rm R}$ and the value predicted from gTMR alone, yielding $f_{\rm R,IZR}$. Analogous to gTMR, it is represented by the "IZR-induced component of the $\hat{g}$ derivative," $\hat{g}'_{\rm IZR}$.

Rabi driving arising from a mixture of both mechanisms is described by [33]

$$\mathbf{f}_{\rm R} = \frac{\mu_{\rm B} V_{\rm MW} |\mathbf{B}|}{2h} [\mathbf{n} \times (\hat{g}'\mathbf{b})], \quad \mathbf{b} = \frac{\mathbf{B}}{|\mathbf{B}|}. \tag{2}$$

Here, $\mathbf{f}_{\rm R}$ defines the Rabi vector, whose magnitude gives the Rabi frequency $f_{\rm R} = |\mathbf{f}_{\rm R}|$, while its direction corresponds to the axis of spin rotation on the Bloch sphere. The quantity $\hat{g}' = \hat{g}'_{\rm gTMR} + \hat{g}'_{\rm IZR}$ denotes the derivative of the g tensor with respect to the gate voltage on the driving electrode, with contributions from gTMR and IZR. The term $\hat{g}'\mathbf{b}$ represents the oscillating effective magnetic field, and the cross product with the spin-quantization axis $\mathbf{n}$ ensures that only components perpendicular to the static Zeeman field contribute to the Rabi drive. Note that both driving mechanisms scale linearly with the electric- and magnetic-field amplitudes, and therefore cannot be separated without analyzing their distinct angular dependencies (Sec. D of the Supplemental Material [52]).

C. Extraction of *g* tunability and full Rabi-model reconstruction

Next, we determine $\hat{g}'_{\rm gTMR}$ and $\hat{g}'_{\rm IZR}$ following the method of Crippa *et al.* [33] (Sec. E of the Supplemental Material [52]). We begin by measuring how $E_{\rm Z}$ changes with the voltage applied to the driving gate [Fig. 2(c)], yielding the longitudinal g-factor tunability $\frac{\partial E_Z}{\partial V} = \mu_{\rm B} B g'_{\parallel}$, where $g'_{\parallel} = \frac{\partial |\hat{g}\mathbf{b}|}{\partial V} = [\hat{g}'\mathbf{b}] \cdot \mathbf{n}$. Here, $g'_{\parallel}$ quantifies the voltage-induced change in the magnitude of the effective Zeeman field, i.e., its component along the spin-quantization axis. Consequently, $g'_{\parallel}$ modulates the Zeeman splitting without tilting $\mathbf{n}$, producing dephasing rather than coherent rotations. Because IZR leaves $E_{\rm Z}$ invariant, it contributes no longitudinal response, so $\hat{g}'_{\rm IZR,\parallel} = 0$. Thus, the measured $g'_{\parallel}$ reflects only the gTMR contribution, enabling a reconstruction of $\hat{g}'_{\rm gTMR}$—up to the usual unitary freedom in the choice of spin basis—for driving from gates P1 and B [33]. Projecting the fitted $\hat{g}'_{\rm gTMR}$ onto the spin-quantization axis and magnetic-field orientation according to $g'_{\parallel} = [\hat{g}'_{\rm gTMR}\mathbf{b}] \cdot \mathbf{n}$ reproduces the measured data with good agreement [Fig. 2(c), solid curves], thereby validating the reconstruction.

The transverse component of this tensor governs coherent Rabi driving by gTMR and is given by $g'_{\rm gTMR,\perp} = |[\hat{g}'_{\rm gTMR}\mathbf{b}] \times \mathbf{n}|$. By comparing the predicted $f_{\rm R,gTMR}$ with the measured $f_{\rm R}$, the remaining contribution can be attributed to IZR, which allows extraction of $\hat{g}'_{\rm IZR}$ [33]. By definition, $\hat{g}'_{\rm IZR}$ has no longitudinal component but a finite transverse response $g'_{\rm IZR,\perp} = |[\hat{g}'_{\rm IZR}\mathbf{b}] \times \mathbf{n}|$, leading to coherent spin rotations.

Utilizing Eq. (2) together with the determined $\hat{g}' = \hat{g}'_{\rm gTMR} + \hat{g}'_{\rm IZR}$, we obtain a model that incorporates both driving mechanisms and is fully consistent with the measured angular dependence of the Rabi frequency [Fig. 2(b), solid curves]. The matrices for driving from P1 are

$$\hat{g}'^{\rm P1}_{\rm gTMR} = \begin{pmatrix} -0.36 & 1.52 & 0.31 \\ 1.55 & -0.71 & -0.35 \\ 0.35 & -0.37 & -0.87 \end{pmatrix} {\rm V}^{-1}, \tag{3}$$

$$\hat{g}'^{\rm P1}_{\rm IZR} = \begin{pmatrix} 0.006 & 0.019 & -0.163 \\ -0.022 & -0.004 & 0.049 \\ -0.300 & -0.015 & -0.002 \end{pmatrix} {\rm V}^{-1}, \tag{4}$$

and for driving from B are

$$\hat{g}'^{\rm B}_{\rm gTMR} = \begin{pmatrix} 0.62 & -1.01 & -0.40 \\ -1.03 & 0.71 & 0.27 \\ -0.47 & 0.16 & 0.20 \end{pmatrix} {\rm V}^{-1}, \tag{5}$$

$$\hat{g}'^{\rm B}_{\rm IZR} = \begin{pmatrix} -0.015 & 0.118 & 0.725 \\ -0.071 & -0.038 & -0.681 \\ -0.832 & 0.717 & 0.053 \end{pmatrix} {\rm V}^{-1}. \tag{6}$$

We now compare the g-factor tunability when driving from gates P1 and B. Across the two drive configurations, $g'_{\parallel}$ shows an angular dependence that is mirrored about zero [Fig. 2(c), solid curves]. In contrast, $g'_{\rm gTMR,\perp}$ follows a similar angular trend for both drive configurations [Fig. 2(d), solid curves]. Notably, the magnitudes of $g'_{\parallel}$ and $g'_{\rm gTMR,\perp}$ are generally smaller under B driving [Figs. 2(c) and 2(d), orange curves) than under P1 driving (blue curves), which is counterintuitive given the larger gate lever arm of gate B $\alpha^{\rm B} = 0.208 \pm 0.005$ versus $\alpha^{\rm P1} = 0.125 \pm 0.002$, indicating stronger electric-field coupling. Conversely, B driving results in a much larger $g'_{\rm IZR,\perp}$ [Fig. 2(d), orange dotted curves] compared to P1 driving (blue dotted curves). This finding highlights the nontrivial nature of g tuning by gate voltages, as it pertains to effects beyond simple capacitive couplings.

D. Tuning the EDSR drive composition

Our model enables a quantitative comparison of the driving contributions from the two mechanisms under P1 or B driving by computing the Rabi vector $\mathbf{f}_{\rm R}$ and its components $\mathbf{f}_{\rm R,IZR}$ and $\mathbf{f}_{\rm R,gTMR}$ for all magnetic-field orientations (see Fig. 3). The latter two "pure" contributions are obtained directly from

TABLE I. Drive contributions for Q1.

	$p_{\mathrm{IZR}}^{\mathrm{Q1}}$	$p_{\mathrm{gTMR}}^{\mathrm{Q1}}$
P1 drive	15%	85%
B drive	55%	45%

Eq. (2) by substituting $\hat{g}'$ with the corresponding matrix for each driving mechanism. Since the total Rabi vector is given by $\mathbf{f}_{\mathrm{R}} = \mathbf{f}_{\mathrm{R,IZR}} + \mathbf{f}_{\mathrm{R,gTMR}}$, their magnitudes satisfy the triangle inequality $f_{\mathrm{R}} \leqslant f_{\mathrm{R,IZR}} + f_{\mathrm{R,gTMR}}$. The two contributions add vectorially and, depending on their relative orientation, may interfere constructively, destructively, or anywhere in between. From the calculated maps of $f_{\mathrm{R,gTMR}}$ and $f_{\mathrm{R,IZR}}$, it is evident that gTMR dominates the Rabi driving under P1 driving, whereas B driving produces a markedly different pattern, with both mechanisms contributing significantly and exhibiting distinct anisotropies.

To quantify this observation, we define the average fractional contribution of each mechanism as

$$p_{\mathrm{IZR}} = \frac{\langle|\mathbf{f}_{\mathrm{R,IZR}}|\rangle}{\mathcal{F}}, \quad p_{\mathrm{gTMR}} = \frac{\langle|\mathbf{f}_{\mathrm{R,gTMR}}|\rangle}{\mathcal{F}}, \tag{7}$$

$$\mathcal{F} = \langle|\mathbf{f}_{\mathrm{R,IZR}}|\rangle + \langle|\mathbf{f}_{\mathrm{R,gTMR}}|\rangle, \tag{8}$$

where $\langle|\mathbf{x}|\rangle$ denotes the average magnitude of $\mathbf{x}$ over all magnetic-field orientations, i.e., over the solid angle of the unit sphere. The results are presented in Table I, confirming the conclusions drawn above.

Thus, selecting different gate electrodes enables *in situ* control over the relative contributions of the two EDSR driving mechanisms. Notably, the maximum $f_{\mathrm{R,IZR}}$ increases from below 4 MHz under P1 driving to above 20 MHz under B driving—a fivefold enhancement achieved by laterally shifting the drive source by only $\simeq 30$ nm. This demonstrates a high degree of tunability and highlights the potential for further optimization of the device geometry to tailor the spin-driving mechanism.

IV. DISCUSSION

A. Future directions based on drive tuning

Our findings motivate experiments beyond the fundamental physics described here. Switching the driving gate offers an electrical means of local control that can be executed much faster than rotating the magnetic field [33]. In principle, such electrical control could be automated [56,57] and carried out adaptively using fast feedback [11], enabling real-time adjustment of the driving mechanism.

This could be exploited to implement an all-electric toggle between fast qubit drive ($f_{\mathrm{R}} \geqslant 10$ MHz) and an idle position ($f_{\mathrm{R}} \simeq 0$ MHz) [22], simply by relaying an always-on radio frequency drive signal to P1 instead of B, e.g., using on-chip multiplexing [58]. A possible operation point can be seen in Fig. 3 near $\theta \simeq 165^\circ, \phi \simeq 135^\circ$. This scheme could remove the need for engineered drive pulses with sub-nanosecond rise times, relaxing the high-frequency hardware requirements [45].

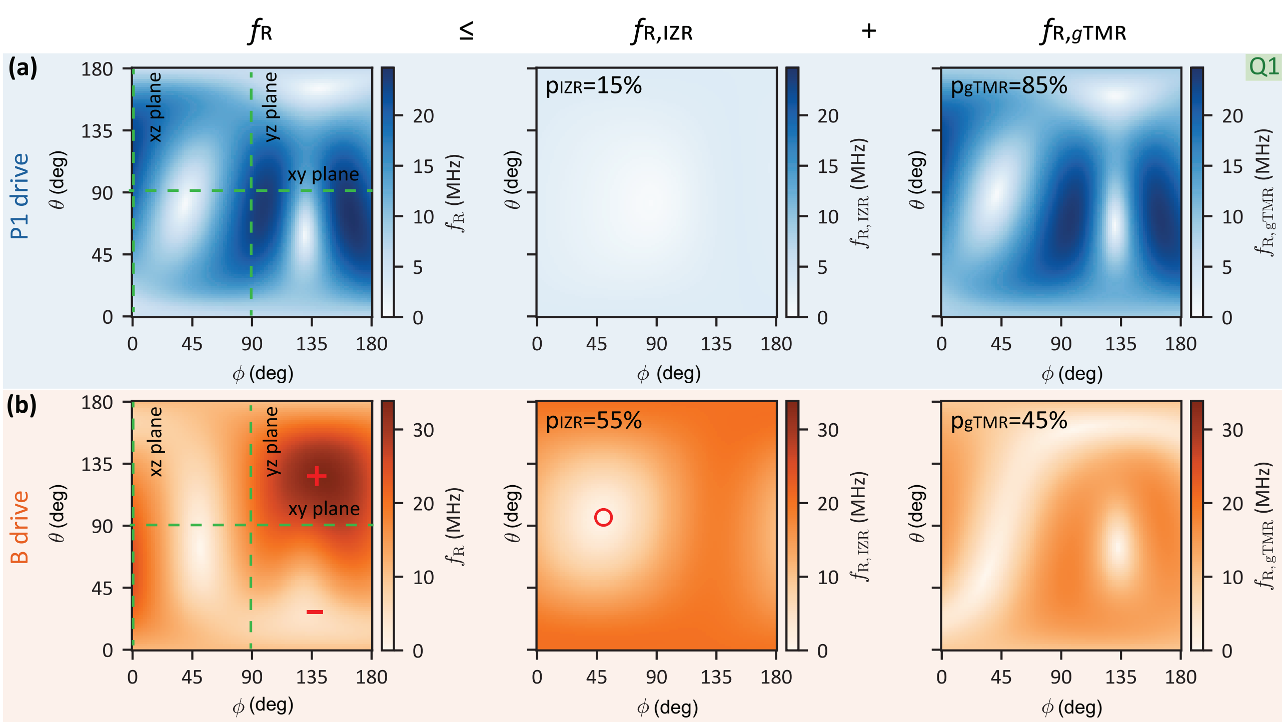

FIG. 3. IZR and gTMR Rabi drive contributions. (a) Calculated Rabi frequency of Q1 (first column), decomposed into the contributions from IZR (second column) and gTMR (third column) under P1 driving. The dominant contribution arises from gTMR, with $p_{\mathrm{gTMR}} = 85\%$. (b) Same analysis for B driving. Here, IZR and gTMR contribute comparably to the total Rabi driving ($p_{\mathrm{IZR}} = 55\%$ and $p_{\mathrm{gTMR}} = 45\%$). Constructive (destructive) interference between the two mechanisms occurs at the red + (−) symbols, leading to enhanced (suppressed) overall Rabi frequency.

Furthermore, the same drive tone could be applied simultaneously to both the B and P1 gates [51,55]. By controlling the relative amplitudes and phases on the two gates, one could smoothly explore the drive mechanism transition. The same strategy could be used to compensate rf leakage between neighboring gates, which we estimate around 15%–20% for our devices due to residual capacitive crosstalk [44,59,60].

Such experiments would require detailed knowledge of the qubit's anisotropies and drive mechanism landscape, traditionally causing a large overhead for precharacterization of every single qubit. Recently developed, fully autonomous protocols for the extraction of f_R and g^* [56] with fast radio-frequency-based readout [57] are able to streamline and speed up this process significantly.

B. Link between electric-field orientation and driving mechanism

Experimental insights into the local microwave fields in semiconducting nanostructures are notoriously difficult to acquire and validate. Our results show that a nanometer-scale displacement of the driving source profoundly impacts the microwave environment at the QD's location, manifesting itself as a changed drive composition. The findings are straightforwardly interpreted. Q1 is located mostly beneath P1; thus, driving from P1 primarily generates out-of-plane electric-field lines, which mainly deform the confinement potential and therefore favor gTMR. In contrast, gate B is laterally offset from the qubit, producing at Q1 an ac electric field that contains not only a vertical component but also a substantial in-plane component along the fin—the direction of weak confinement. This naturally results in an enhanced IZR contribution, supporting intuition [40].

We note that the IZR contribution found from B driving of Q2 ($p_{\mathrm{IZR}}^{\mathrm{Q2}} = 72\%$) shown in Sec. F of the Supplemental Material [52] is much higher than for Q1, indicating overall asymmetry between the two dots. Surprisingly, when Q2 is driven from the even more remote gate P1, the IZR contribution is again reduced to $p_{\mathrm{IZR}}^{\mathrm{Q2}} = 57\%$. We believe that the staggered gate structure where B is much closer to the Si fin than P1 and P2 due to the oxide separating the two gate layers may cause additional shielding and result in counterintuitive field directions when the drive is applied to a remote gate as is the case for P1 driving of Q2.

C. Qubit operation under IZR and gTMR

A qubit's gate speed is determined by its f_R, and multiqubit operation is limited by the slowest participating qubit. It is thus essential to avoid configurations where individual qubits have vanishing f_R when scaling to larger qubit arrays [4,8,61]. As evident from Fig. 3 and previous reports [20,33], gTMR exhibits multiple magnetic-field orientations where $f_R \simeq 0$, while IZR has only one slow spot, namely, where $\mathbf{B} \parallel \mathbf{n}_{\mathrm{SO}}$ [23,39,62]. As a consequence, ensuring homogeneously high gate speeds across larger qubit arrays may be facilitated by IZR driving without demanding qubit-specific tuning typically required for gTMR-driven systems [20].

The qubit's coherence is of equal importance for practical qubit operation. Simultaneous optimization of a hole spin's speed and coherence can be achieved electrostatically [20,40] or by choosing an optimal magnetic-field direction [17,20]. Our FinFET qubit's dephasing time T_2^* varies strongly with the orientation of **B** (see Fig. S4 of the Supplemental Material [52], Ref. [63] for the coherence model, and Refs. [64,65] for noise benchmarks). Interestingly, the gTMR-dominated drive from P1 shows enhanced T_2^* and f_R for some field directions ($\theta \simeq 120^\circ, \phi \simeq 10^\circ$) but the local maxima of T_2^* and f_R are not perfectly aligned. Conversely, the fastest Rabi driving achieved with B driving and mixed drive mechanisms ($\theta \simeq 120^\circ, \phi \simeq 135^\circ$) lies far away from any coherence sweet spot. This may indicate that "reciprocal sweetness" [20,41,42] is more straightforwardly realized in gTMR driving.

V. CONCLUSION

In conclusion, we have demonstrated *in situ* all-electric control over the Rabi drive mechanisms of a hole-spin qubit in an Si FinFET. By mapping the g tensor, its derivatives with respect to plunger- and barrier-gate voltages, and the Rabi frequency, and fitting all quantities using the g-matrix formalism, we obtain a quantitative description of the underlying driving composition. When the drive is applied to the plunger gate P1, the qubit is predominantly driven via gTMR. In contrast, driving from the barrier gate B yields a more balanced composition, with significant contributions from both gTMR and IZR. Switching from P1 to B driving enhances the IZR-induced Rabi speed by a factor of 5. These findings suggest that the driving field orientation at the qubit is governed by the spatial arrangement of the driving gate and the QD, providing experimental access to the device's microscopic microwave environment.

VI. OUTLOOK

The demonstration of drive switching motivates more extensive studies of different drive modalities on the qubit performance along the entire spectrum of spin-qubit operations such as idling, shuttling [66,67], resonator coupling [68–72], two-qubit gates [11,14,19], and readout [73,74]. This may also inform optimized gate electrode designs and choice of the driving gate, tailored to promote gTMR, IZR, or an even mixture.

Furthermore, it remains to be seen whether a more complete inversion of the drive composition—i.e., a transition from $p_{\mathrm{gTMR}} \gg p_{\mathrm{IZR}}$ to $p_{\mathrm{gTMR}} \ll p_{\mathrm{IZR}}$—can be achieved. This may be possible by applying the drive to the right plunger gate (P2), or to a gate electrode positioned even more laterally offset along the fin. Our attempts at driving the qubit from P2 were unsuccessful, likely due to a technical failure of the measurement setup, also preventing the investigation of P2 driving of Q2.

ACKNOWLEDGMENTS

We thank T. Berger, L. Camenzind, S. Bosco, and T. Patlatiuk for useful discussions and experimental support. We acknowledge the support of the cleanroom operation team, particularly U. Drechsler, A. Olziersky, and D. D. Pineda, at the IBM Binnig and Rohrer Nanotechnology Center, as well as technical assistance at the University of Basel by S. Martin and M. Steinacher. This work was supported by NCCR SPIN, a National Center of Competence in Research funded by the Swiss National Science Foundation (Grant No. 225153). A.V.K. and P.S. acknowledge funding within the QuantERA II program, which received support from the EU's Horizon 2020 research and innovation program under Grant Agreement No. 101017733.

S.G., C.D.S., R.S.E., and A.V.K. performed the experiments and analyzed the data with input from R.J.W. and D.M.Z. S.G., R.S.E., and A.V.K. wrote the manuscript with contributions from all authors. M.J.C., P.S., and D.L. provided valuable input on the conceptual understanding and theoretical analysis. S.G. and A.V.K. conceived the project. A.V.K. managed the project with support from R.J.W. and D.M.Z.

DATA AVAILABILITY

The data supporting this study are available in a Zenodo repository [75].

[1] G. Burkard, T. D. Ladd, A. Pan, J. M. Nichol, and J. R. Petta, Semiconductor spin qubits, Rev. Mod. Phys. **95**, 025003 (2023).

[2] D. Loss and D. P. DiVincenzo, Quantum computation with quantum dots, Phys. Rev. A **57**, 120 (1998).

[3] D. V. Bulaev and D. Loss, Spin relaxation and decoherence of holes in quantum dots, Phys. Rev. Lett. **95**, 076805 (2005).

[4] S. G. J. Philips, M. T. Mądzik, S. V. Amitonov, S. L. de Snoo, M. Russ, N. Kalhor, C. Volk, W. I. L. Lawrie, D. Brousse, L. Tryputen, B. P. Wuetz, A. Sammak, M. Veldhorst, G. Scappucci, and L. M. K. Vandersypen, Universal control of a six-qubit quantum processor in silicon, Nature (London) **609**, 919 (2022).

[5] M. F. Gonzalez-Zalba, S. de Franceschi, E. Charbon, T. Meunier, M. Vinet, and A. S. Dzurak, Scaling silicon-based quantum computing using CMOS technology, Nat. Electron. **4**, 872 (2021).

[6] A. J. Weinstein, M. D. Reed, A. M. Jones, R. W. Andrews, D. Barnes, J. Z. Blumoff, L. E. Euliss, K. Eng, B. H. Fong, S. D. Ha, *et al.*, Universal logic with encoded spin qubits in silicon, Nature (London) **615**, 817 (2023).

[7] S. Neyens, O. K. Zietz, T. F. Watson, F. Luthi, A. Nethwewala, H. C. George, E. Henry, M. Islam, A. J. Wagner, F. Borjans, *et al.*, Probing single electrons across 300-mm spin qubit wafers, Nature (London) **629**, 80 (2024).

[8] H. C. George, M. T. Mądzik, E. M. Henry, A. J. Wagner, M. M. Islam, F. Borjans, E. J. Connors, J. Corrigan, M. Curry, M. K. Harper, *et al.*, 12-spin-qubit arrays fabricated on a 300 mm semiconductor manufacturing line, Nano Lett. **25**, 793 (2025).

[9] P. Steinacker, N. D. Stuyck, W. H. Lim, T. Tanttu, M. Feng, A. Nickl, S. Serrano, M. Candido, J. D. Cifuentes, F. E. Hudson, *et al.*, Industry-compatible silicon spin-qubit unit cells exceeding 99% fidelity, Nature (London) **646**, 81 (2025).

[10] Y.-H. Wu, L. C. Camenzind, P. Bütler, I. K. Jin, A. Noiri, K. Takeda, T. Nakajima, T. Kobayashi, G. Scappucci, H.-S. Goan, and S. Tarucha, Simultaneous high-fidelity single-qubit gates in a spin qubit array, arXiv:2507.11918.

[11] J. Y. Huang, R. Y. Su, W. H. Lim, M. Feng, B. van Straaten, B. Severin, W. Gilbert, N. Dumoulin Stuyck, T. Tanttu, *et al.*, High-fidelity spin qubit operation and algorithmic initialization above 1 K, Nature (London) **627**, 772 (2024).

[12] R. Maurand, X. Jehl, D. Kotekar-Patil, A. Corna, H. Bohuslavskyi, R. Laviéville, L. Hutin, S. Barraud, M. Vinet, M. Sanquer, and S. D. Franceschi, A CMOS silicon spin qubit, Nat. Commun. **7**, 13575 (2016).

[13] N. W. Hendrickx, W. I. L. Lawrie, L. Petit, A. Sammak, G. Scappucci, and M. Veldhorst, A single-hole spin qubit, Nat. Commun. **11**, 3478 (2020).

[14] N. Hendrickx, D. Franke, A. Sammak, G. Scappucci, and M. Veldhorst, Fast two-qubit logic with holes in germanium, Nature (London) **577**, 487 (2020).

[15] N. W. Hendrickx, W. I. L. Lawrie, M. Russ, F. van Riggelen, S. L. de Snoo, R. N. Schouten, A. Sammak, G. Scappucci, and M. Veldhorst, A four-qubit germanium quantum processor, Nature (London) **591**, 580 (2021).

[16] L. C. Camenzind, S. Geyer, A. Fuhrer, R. J. Warburton, D. M. Zumbühl, and A. V. Kuhlmann, A hole spin qubit in a fin field-effect transistor above 4 kelvin, Nat. Electron. **5**, 178 (2022).

[17] N. Piot, B. Brun, V. Schmitt, S. Zihlmann, V. P. Michal, A. Apra, J. C. Abadillo-Uriel, X. Jehl, B. Bertrand, H. Niebojewski, L. Hutin, M. Vinet, M. Urdampilleta, T. Meunier, Y.-M. Niquet, R. Maurand, and S. D. Franceschi, A single hole spin with enhanced coherence in natural silicon, Nat. Nanotechnol. **17**, 1072 (2022).

[18] N. W. Hendrickx, L. Massai, M. Mergenthaler, F. J. Schupp, S. Paredes, S. W. Bedell, G. Salis, and A. Fuhrer, Sweet-spot operation of a germanium hole spin qubit with highly anisotropic noise sensitivity, Nat. Mater. **23**, 920 (2024).

[19] S. Geyer, B. Hetényi, S. Bosco, L. C. Camenzind, R. S. Eggli, A. Fuhrer, D. Loss, R. J. Warburton, D. M. Zumbühl, and A. V. Kuhlmann, Anisotropic exchange interaction of two hole-spin qubits, Nat. Phys. **20**, 1152 (2024).

[20] M. Bassi, E.-A. Rodrıguez-Mena, B. Brun, S. Zihlmann, T. Nguyen, V. Champain, J. C. Abadillo-Uriel, B. Bertrand, H. Niebojewski, R. Maurand, Y.-M. Niquet, X. Jehl, S. De Franceschi, and V. Schmitt, Optimal operation of hole spin qubits, Nat. Phys. **22**, 75 (2026).

[21] I. Vorreiter, J. Y. Huang, S. D. Liles, J. Hillier, R. Li, B. Raes, S. Kubicek, J. Jussot, S. Beyne, C. Godfrin, S. Sharma, D. Wan, N. D. Stuyck, W. Gilbert, C. H. Yang, A. S. Dzurak, K. De Greve, and A. R. Hamilton, Precision high-speed quantum logic with holes on a natural silicon foundry platform, Nat. Commun. (2026), DOI:10.1038/s41467-026-76231-x.

[22] F. N. M. Froning, L. C. Camenzind, O. A. H. van der Molen, A. Li, E. P. A. M. Bakkers, D. M. Zumbühl, and F. R. Braakman, Ultrafast hole spin qubit with gate-tunable spin-orbit switch functionality, Nat. Nanotechnol. **16**, 308 (2021).

[23] V. N. Golovach, M. Borhani, and D. Loss, Electric-dipole-induced spin resonance in quantum dots, Phys. Rev. B **74**, 165319 (2006).

[24] D. V. Bulaev and D. Loss, Electric dipole spin resonance for heavy holes in quantum dots, Phys. Rev. Lett. **98**, 097202 (2007).
[25] C. Kloeffel, M. J. Rančić, and D. Loss, Direct Rashba spin-orbit interaction in Si and Ge nanowires with different growth directions, Phys. Rev. B **97**, 235422 (2018).
[26] S. Bosco, B. Hetényi, and D. Loss, Hole spin qubits in Si FinFETs with fully tunable spin-orbit coupling and sweet spots for charge noise, PRX Quantum **2**, 010348 (2021).
[27] Y. Tokura, W. G. van der Wiel, T. Obata, and S. Tarucha, Coherent single electron spin control in a slanting Zeeman field, Phys. Rev. Lett. **96**, 047202 (2006).
[28] M. Pioro-Ladrière, T. Obata, Y. Tokura, Y.-S. Shin, T. Kubo, K. Yoshida, T. Taniyama, and S. Tarucha, Electrically driven single-electron spin resonance in a slanting Zeeman field, Nat. Phys. **4**, 776 (2008).
[29] W. Gilbert, T. Tanttu, W. H. Lim, M. Feng, J. Y. Huang, J. D. Cifuentes, S. Serrano, P. Y. Mai, R. C. C. Leon, C. C. Escott, K. M. Itoh, N. V. Abrosimov, H.-J. Pohl, M. L. W. Thewalt, F. E. Hudson, A. Morello, A. Laucht, C. H. Yang, A. Saraiva, and A. S. Dzurak, On-demand electrical control of spin qubits, Nat. Nanotechnol. **18**, 131 (2023).
[30] A. Sen, G. Frank, B. Kolok, J. Danon, and A. Pályi, Classification and magic magnetic field directions for spin-orbit-coupled double quantum dots, Phys. Rev. B **108**, 245406 (2023).
[31] M. Sharma and D. P. DiVincenzo, *g*-factor symmetry and topology in semiconductor band states, Proc. Natl. Acad. Sci. USA **121**, e2404298121 (2024).
[32] S. D. Liles, F. Martins, D. S. Miserev, A. A. Kiselev, I. D. Thorvaldson, M. J. Rendell, I. K. Jin, F. E. Hudson, M. Veldhorst, K. M. Itoh, O. P. Sushkov, T. D. Ladd, A. S. Dzurak, and A. R. Hamilton, Electrical control of the *g* tensor of the first hole in a silicon MOS quantum dot, Phys. Rev. B **104**, 235303 (2021).
[33] A. Crippa, R. Maurand, L. Bourdet, D. Kotekar-Patil, A. Amisse, X. Jehl, M. Sanquer, R. Laviéville, H. Bohuslavskyi, L. Hutin, S. Barraud, M. Vinet, Y.-M. Niquet, and S. De Franceschi, Electrical spin driving by *g*-matrix modulation in spin-orbit qubits, Phys. Rev. Lett. **120**, 137702 (2018).
[34] B. Venitucci, L. Bourdet, D. Pouzada, and Y.-M. Niquet, Electrical manipulation of semiconductor spin qubits within the *g*-matrix formalism, Phys. Rev. B **98**, 155319 (2018).
[35] V. P. Michal, B. Venitucci, and Y.-M. Niquet, Longitudinal and transverse electric field manipulation of hole spin-orbit qubits in one-dimensional channels, Phys. Rev. B **103**, 045305 (2021).
[36] N. Ares, G. Katsaros, V. N. Golovach, J. J. Zhang, A. Prager, L. I. Glazman, O. G. Schmidt, and S. D. Franceschi, SiGe quantum dots for fast hole spin Rabi oscillations, Appl. Phys. Lett. **103**, 263113 (2013).
[37] N. Ares, V. N. Golovach, G. Katsaros, M. Stoffel, F. Fournel, L. I. Glazman, O. G. Schmidt, and S. De Franceschi, Nature of tunable hole *g*-factors in quantum dots, Phys. Rev. Lett. **110**, 046602 (2013).
[38] C. E. Pryor and M. E. Flatté, Landé *g*-factors and orbital momentum quenching in semiconductor quantum dots, Phys. Rev. Lett. **96**, 026804 (2006).
[39] K. C. Nowack, F. H. L. Koppens, Y. V. Nazarov, and L. M. K. Vandersypen, Coherent control of a single electron spin with electric fields, Science **318**, 1430 (2007).
[40] M. J. Carballido, S. Svab, R. S. Eggli, T. Patlatiuk, P. Chevalier Kwon, J. Schuff, R. M. Kaiser, L. C. Camenzind, A. Li, N. Ares, E. P. A. M. Bakkers, S. Bosco, J. C. Egues, D. Loss, and D. M. Zumbühl, Compromise-free scaling of qubit speed and coherence, Nat. Commun. **16**, 7616 (2025).
[41] L. Mauro, E. A. Rodríguez-Mena, M. Bassi, V. Schmitt, and Y.-M. Niquet, Geometry of the dephasing sweet spots of spin-orbit qubits, Phys. Rev. B **109**, 155406 (2024).
[42] V. P. Michal, J. C. Abadillo-Uriel, S. Zihlmann, R. Maurand, Y.-M. Niquet, and M. Filippone, Tunable hole spin-photon interaction based on *g*-matrix modulation, Phys. Rev. B **107**, L041303 (2023).
[43] S. Geyer, L. C. Camenzind, L. Czornomaz, V. Deshpande, A. Fuhrer, R. J. Warburton, D. M. Zumbühl, and A. V. Kuhlmann, Self-aligned gates for scalable silicon quantum computing, Appl. Phys. Lett. **118**, 104004 (2021).
[44] R. S. Eggli, T. Patlatiuk, E. G. Kelly, A. Orekhov, G. Salis, R. J. Warburton, D. M. Zumbühl, and A. V. Kuhlmann, Coupling a high-*Q* resonator to a spin qubit with all-electrical control, Phys. Rev. Res. **7**, 013197 (2025).
[45] S. Bosco, S. Geyer, L. C. Camenzind, R. S. Eggli, A. Fuhrer, R. J. Warburton, D. M. Zumbühl, J. C. Egues, A. V. Kuhlmann, and D. Loss, Phase-driving hole spin qubits, Phys. Rev. Lett. **131**, 197001 (2023).
[46] W. G. van der Wiel, S. De Franceschi, J. M. Elzerman, T. Fujisawa, S. Tarucha, and L. P. Kouwenhoven, Electron transport through double quantum dots, Rev. Mod. Phys. **75**, 1 (2002).
[47] K. Ono, D. G. Austing, Y. Tokura, and S. Tarucha, Current rectification by Pauli exclusion in a weakly coupled double quantum dot system, Science **297**, 1313 (2002).
[48] S. Bosco and D. Loss, Fully tunable hyperfine interactions of hole spin qubits in Si and Ge quantum dots, Phys. Rev. Lett. **127**, 190501 (2021).
[49] R. Winkler, *Spin-Orbit Coupling Effects in Two-Dimensional Electron and Hole Systems* (Springer, Berlin, 2003).
[50] I. K. Jin, J. Hillier, S. D. Liles, Z. Wang, A. Shamim, I. Vorreiter, R. Li, C. Godfrin, S. Kubicek, K. D. Greve, D. Culcer, and A. R. Hamilton, Probing *g*-tensor reproducibility and spin-orbit effects in planar silicon hole quantum dots, arXiv:2411.06016.
[51] V. John, F. Borsoi, Z. György, C.-A. Wang, G. Széchenyi, F. van Riggelen-Doelman, W. I. L. Lawrie, N. W. Hendrickx, A. Sammak, G. Scappucci, A. Pályi, and M. Veldhorst, Bichromatic Rabi control of semiconductor qubits, Phys. Rev. Lett. **132**, 067001 (2024).
[52] See Supplemental Material at http://link.aps.org/supplemental/10.1103/f1hx-nk4s for more details on the theory, model and additional experimental results including data for Q2.
[53] Y. Kato, Gigahertz electron spin manipulation using voltage-controlled *g*-tensor modulation, Science **299**, 1201 (2003).
[54] V. John, C. X. Yu, B. van Straaten, E. A. Rodríguez-Mena, M. Rodríguez, S. D. Oosterhout, L. E. A. Stehouwer, G. Scappucci, M. Rimbach-Russ, S. Bosco, F. Borsoi, Y.-M. Niquet, and M. Veldhorst, Robust and localised control of a 10-spin qubit array in germanium, Nat. Commun. **16**, 10560 (2025).
[55] Z. György, A. Pályi, and G. Széchenyi, Limitations of the *g*-tensor formalism of semiconductor spin qubits, Phys. Rev. B **112**, 045428 (2025).

[56] J. Schuff, M. J. Carballido, M. Kotzagiannidis, J. C. Calvo, M. Caselli, J. Rawling, D. L. Craig, B. van Straaten, B. Severin, F. Fedele, S. Svab, P. Chevalier Kwon, R. S. Eggli, T. Patlatiuk, N. Korda, D. M. Zumbühl, and N. Ares, Fully autonomous tuning of a spin qubit, Nat. Electron. **9**, 304 (2026).

[57] C. Carlsson, J. Saez-Mollejo, F. Fedele, S. Calcaterra, D. Chrastina, G. Isella, G. Katsaros, and N. Ares, Automated all-RF tuning for spin qubit readout and control, arXiv:2506.10834.

[58] E. J. Thomas, V. N. Ciriano-Tejel, D. F. Wise, D. Prete, M. d. Kruijf, D. J. Ibberson, G. M. Noah, A. Gomez-Saiz, M. F. Gonzalez-Zalba, M. A. I. Johnson, and J. J. L. Morton, Rapid cryogenic characterization of 1,024 integrated silicon quantum dot devices, Nat. Electron. **8**, 75 (2025).

[59] Q. Ding, A. V. Kuhlmann, A. Fuhrer, and A. Schenk, A generalizable TCAD framework for silicon FinFET spin qubit devices with electrical control, Solid-State Electron. **200**, 108550 (2023).

[60] E. G. Kelly, A. Orekhov, N. W. Hendrickx, M. Mergenthaler, F. J. Schupp, S. Paredes, R. S. Eggli, A. V. Kuhlmann, P. Harvey-Collard, A. Fuhrer, and G. Salis, Capacitive crosstalk in gate-based dispersive sensing of spin qubits, Appl. Phys. Lett. **123**, 262104 (2023).

[61] I. Seidler, B. Hetényi, L. Sommer, L. Massai, K. Tsoukalas, E. G. Kelly, A. Orekhov, M. Aldeghi, S. W. Bedell, S. Paredes, F. J. Schupp, M. Mergenthaler, G. Salis, A. Fuhrer, and P. Harvey-Collard, Spatial uniformity of g-tensor and spin-orbit interaction in germanium hole spin qubits, arXiv:2510.03125.

[62] S. D. Liles, D. J. Halverson, Z. Wang, A. Shamim, R. S. Eggli, I. K. Jin, J. Hillier, K. Kumar, I. Vorreiter, M. J. Rendell, J. Y. Huang, C. C. Escott, F. E. Hudson, W. H. Lim, D. Culcer, A. S. Dzurak, and A. R. Hamilton, A singlet-triplet hole-spin qubit in MOS silicon, Nat. Commun. **15**, 7690 (2024).

[63] T. Tanttu, B. Hensen, K. W. Chan, C. H. Yang, W. W. Huang, M. Fogarty, F. Hudson, K. Itoh, D. Culcer, A. Laucht, A. Morello, and A. Dzurak, Controlling spin-orbit interactions in silicon quantum dots using magnetic field direction, Phys. Rev. X **9**, 021028 (2019).

[64] E. Paladino, Y. M. Galperin, G. Falci, and B. L. Altshuler, $1/f$ noise: Implications for solid-state quantum information, Rev. Mod. Phys. **86**, 361 (2014).

[65] A. Elsayed, M. M. K. Shehata, C. Godfrin, S. Kubicek, S. Massar, Y. Canvel, J. Jussot, G. Simion, M. Mongillo, D. Wan, B. Govoreanu, I. P. Radu, R. Li, P. Van Dorpe, and K. De Greve, Low charge noise quantum dots with industrial CMOS manufacturing, npj Quantum Inf. **10**, 70 (2024).

[66] S. Bosco, J. Zou, and D. Loss, High-fidelity spin qubit shuttling via large spin-orbit interactions, PRX Quantum **5**, 020353 (2024).

[67] T. Struck, M. Volmer, L. Visser, T. Offermann, R. Xue, J.-S. Tu, S. Trellenkamp, L. Cywiński, H. Bluhm, and L. R. Schreiber, Spin-EPR-pair separation by conveyor-mode single electron shuttling in Si/SiGe, Nat. Commun. **15**, 1325 (2024).

[68] X. Mi, M. Benito, S. Putz, D. M. Zajac, J. M. Taylor, G. Burkard, and J. R. Petta, A coherent spin–photon interface in silicon, Nature (London) **555**, 599 (2018).

[69] N. Samkharadze, G. Zheng, N. Kalhor, D. Brousse, A. Sammak, U. C. Mendes, A. Blais, G. Scappucci, and L. M. K. Vandersypen, Strong spin-photon coupling in silicon, Science **359**, 1123 (2018).

[70] A. J. Landig, J. V. Koski, P. Scarlino, U. C. Mendes, A. Blais, C. Reichl, W. Wegscheider, A. Wallraff, K. Ensslin, and T. Ihn, Coherent spin–photon coupling using a resonant exchange qubit, Nature (London) **560**, 179 (2018).

[71] J. Dijkema, X. Xue, P. Harvey-Collard, M. Rimbach-Russ, S. L. de Snoo, G. Zheng, A. Sammak, G. Scappucci, and L. M. K. Vandersypen, Cavity-mediated iswap oscillations between distant spins, Nat. Phys. **21**, 168 (2025).

[72] C. X. Yu, S. Zihlmann, J. C. Abadillo-Uriel, V. P. Michal, N. Rambal, H. Niebojewski, T. Bedecarrats, M. Vinet, E. Dumur, M. Filippone, B. Bertrand, S. De Franceschi, Y.-M. Niquet, and R. Maurand, Strong coupling between a photon and a hole spin in silicon, Nat. Nanotechnol. **18**, 741 (2023).

[73] G. A. Oakes, V. N. Ciriano-Tejel, D. F. Wise, M. A. Fogarty, T. Lundberg, C. Lainé, S. Schaal, F. Martins, D. J. Ibberson, L. Hutin, *et al.* Fast high-fidelity single-shot readout of spins in silicon using a single-electron box, Phys. Rev. X **13**, 011023 (2023).

[74] H. Kiyama, D. van Hien, A. Ludwig, A. D. Wieck, and A. Oiwa, High-fidelity spin readout via the double latching mechanism, npj Quantum Inf. **10**, 95 (2024).

[75] Supporting data for "*In situ* control of hole-spin driving mechanisms" [Dataset], Zenodo, 2026, https://doi.org/10.5281/zenodo.20273647.